PHOTONICS Research

Magnetically tunable zero-index metamaterials

Yucong Yang,[1,2] Yueyang Liu,[3] Jun Qin,[1,2] Songgang Cai,[1,2] Jiejun Su,[1,2] Peiheng Zhou,[1,2] Longjiang Deng,[1,2,4] Yang Li,[3,5] and Lei Bi[1,2,6]

[1]National Engineering Research Centre of Electromagnetic Radiation Control Materials, University of Electronic Science and Technology of China, Chengdu 611731, China
[2]Key Laboratory of Multi-spectral Absorbing Materials and Structures of Ministry of Education, University of Electronic Science and Technology of China, Chengdu 611731, China
[3]State Key Laboratory of Precision Measurement Technology and Instrument, Department of Precision Instrument, Tsinghua University, Beijing 100084, China
[4]e-mail: denglj@uestc.edu.cn
[5]e-mail: yli9003@mail.tsinghua.edu.cn
[6]e-mail: bilei@uestc.edu.cn

Zero-index metamaterials (ZIMs) feature a uniform electromagnetic mode over a large area in arbitrary shapes, enabling many applications including high-transmission supercouplers with arbitrary shapes, direction-independent phase matching for nonlinear optics, and collective emission of many quantum emitters. However, most ZIMs reported to date are passive; active ZIMs that allow for dynamic modulation of their electromagnetic properties have rarely been reported. Here, we design and fabricate a magnetically tunable ZIM consisting of yttrium iron garnet (YIG) pillars sandwiched between two copper clad laminates in the microwave regime. By harnessing the Cotton–Mouton effect of YIG, the metamaterial was successfully toggled between gapless and bandgap states, leading to a "phase transition" between a zero-index phase and a single negative phase of the metamaterial. Using an S-shaped ZIM supercoupler, we experimentally demonstrated a tunable supercoupling state with a low intrinsic loss of 0.95 dB and a high extinction ratio of up to 30.63 dB at 9 GHz. We have also engineered a transition between the supercoupling state and the topological one-way transmission state at 10.6 GHz. Our work enables dynamic modulation of the electromagnetic characteristics of ZIMs, enabling various applications in tunable linear, nonlinear, quantum, and nonreciprocal electromagnetic devices.   © 2023 Chinese Laser Press

https://doi.org/10.1364/PRJ.495638

1. INTRODUCTION

Zero-index materials (ZIMs) are materials or composite structures that exhibit an effective refractive index of zero at a given frequency [1–4], resulting in an infinite spatial wavelength. This effect can be leveraged to overcome the limitations imposed by the finite spatial wavelength of electromagnetic waves, thereby enabling various novel physical phenomena and applications in linear [5–7], nonlinear [8–10], and quantum electromagnetic systems [11,12]. Although the concept of zero-index materials was proposed a long time ago [13], zero-index materials, such as indium tin oxide [9,14,15], waveguides at cut-off frequencies [16–18], fishnet metamaterials [19], and doped ε-near-zero (ENZ) media [20] did not garner too much research interest until around 2010 [2]. However, the aforementioned materials and artificial structures exhibit large ohmic losses because of their metallic components [21]. In contrast, ZIMs based on all-dielectric photonic crystals exhibit zero ohmic loss, enabling the realization of ZIMs over a large area of arbitrary shapes. A photonic-crystal-based ZIM was first realized in the microwave regime based on Al_2O_3 pillars embedded in a parallel metal waveguide [22]. Subsequently, photonic-crystal-based ZIMs ranging from acoustic [23,24] to photonic regimes [25–29] have been reported, demonstrating fascinating physical phenomena and applications, such as supercoupling [4,30], leaky-wave antennas [31], cloaking [22,32–35], superradiance [12,25], and phase matching with multiple configurations of input and output waves for nonlinear optics [10]. For the applications in superradiance and nonlinear optics, although photonic-crystal-based ZIMs do not show strong field enhancement which can be provided by the slow-light effect of ENZ media [13,36–38], photonic-crystal-based ZIMs' finite impedance and absence of ohmic loss can still reduce the pump power dramatically.

Despite this progress, most of the ZIMs reported thus far are passive, with constant post-fabrication electromagnetic properties, limiting their applications in passive devices. As a consequence, there have been substantial efforts to implement active ZIMs with tunable magnetic (μ_{eff}) and electric (ε_{eff})

properties using external stimuli [39,40]. One particular tunable system is magnetically tunable ZIM [41], which is essentially different from electrically, thermally, and other tunable ZIMs [42–44], photonic crystals [45–48], metasurfaces [49], and transparent conductive oxide (TCO) materials [9]. Such a system was first proposed by Davoyan *et al.* theoretically [41]. In their proposal, unique properties such as "Hall opacity" and "Hall transparency," can be observed under applied magnetic field, indicating magnetic-field-induced opacity or transparency. Since then, much theoretical progress on magnetic ZIMs has been achieved [50–53]. Despite this progress, to the best of our knowledge, no experimental work on magnetic ZIMs has been demonstrated to date. In turn, this intriguing mechanism is also expected to enable energy-efficient modulation of electromagnetic wave propagation with low insertion loss, high extinction ratio, and compact device footprint—which are all essential factors in microwave and optical communication applications [3,20,54,55].

In this study, we design and experimentally investigate a magnetically tunable ZIM consisting of an array of gyromagnetic pillars embedded within a parallel-plate copper waveguide. Under an applied magnetic field of 430 Oe, the photonic band structure of the proposed ZIM changes from a zero-index state to a photonic bandgap state, corresponding to a transition from a "zero-index phase" to a "single negative phase." Based on this property, we propose a magnetic field-induced on–off switch of the supercoupling state in an S-shaped ZIM waveguide, resulting in a low intrinsic loss of 0.95 dB and a high extinction ratio of 30.63 dB at 9 GHz. We also demonstrate a magnetic-field-controlled switch to effect transitions between a zero-index state and a nontrivial topological boundary state in the magnetic ZIM. In addition, we also present another device design, showing a much higher extinction ratio up to 104 dB. These results demonstrate the potential of applying active ZIMs in RF ferrite switches, ultra-compact ferrite phase shifters, electromagnetic wave modulators, and some other nonreciprocal devices.

2. RESULTS

A. Design of Magnetically Tunable Zero-Index Metamaterials

First, we designed a Dirac-like cone-based zero-index metamaterial (DCZIM) consisting of a square array of dielectric pillars embedded in a parallel-plate copper waveguide [22]. At the Γ point, the accidental degeneracy of two linear dispersion bands and a quadratic dispersion band formed a Dirac-like cone dispersion, corresponding to an impedance-matched zero effective index [22]. In contrast to conventional passive ZIMs, we achieved active modulation by fabricating a square lattice of pillars constructed using a magnetic dielectric material, yttrium iron garnet (YIG). By applying a magnetic field to the YIG pillars along the direction perpendicular to the wave vector of the transverse magnetic (TM) mode, an effective permeability modulation that is quadratically proportional to the YIG magnetization was observed owing to the Cotton–Mouton effect (see Appendix B for further details). In turn, this effect enabled the modulation of the photonic band structure and the effective index of metamaterials.

We implemented the proposed design using the structure depicted in Fig. 1. Figure 1(a) illustrates the experimentally fabricated metamaterial consisting of a square lattice of gyromagnetic YIG pillars with a 3.53 mm radius and a 17.9 mm lattice constant. The dielectric constant [56] and permeability of the YIG material were characterized (see Appendices A and C for further details). The YIG pillars were placed in a waveguide consisting of two parallel copper clad laminates separated by 4 mm. A magnetic field was applied to each YIG pillar by placing a neodymium iron boron (NdFeB) permanent magnet under each pillar and behind the copper back plate. A uniform magnetic field along the z-direction was observed, whose intensity reached 430 Oe in the middle of the two copper clad laminates. This was sufficient to saturate the YIG pillars (see Appendix C for further details).

B. Experimental Observation of Photonic Band Structure

To characterize the properties of DCZIM, we first calculated and then experimentally measured the photonic band structure in the plane of the YIG array. The gray dotted line in Fig. 2(a) represents the calculated band structure for the TM modes (the electric field is polarized in the z direction) of this photonic crystal, as observed based on a simulation using COMSOL Multiphysics. We observed a clear Dirac-like cone dispersion at 9 GHz. When a magnetic field of +430 Oe was applied along the z direction, the off-diagonal component induced the Cotton–Mouton effect in YIG, changing the
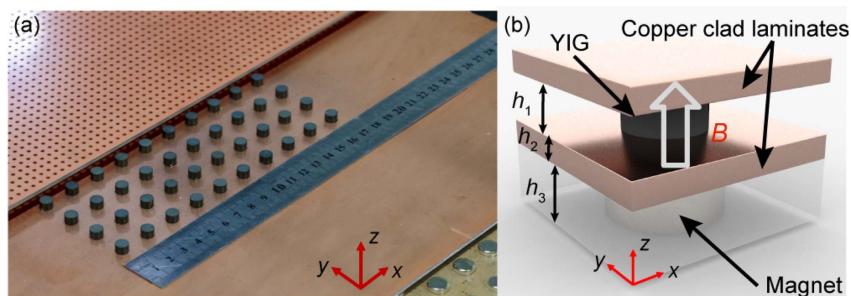

Fig. 1. Schematic diagram of the active DCZIM structure. (a) The structure of an active DCZIM based on a gyromagnetic photonic crystal. (b) Schematic diagram of a unit cell. The YIG pillars were placed in a parallel-plate copper-clad waveguide with height $h_1 = 4$ mm. The thickness of the waveguide plates was $h_2 = 2$ mm. Permanent magnets with 5 mm diameter and height $h_3 = 5$ mm were placed in an acrylic matrix underneath the waveguide and were aligned with the YIG pillars.

frequencies of the three photonic bands forming the Dirac-like cone. Owing to time reversal symmetry (TRS) breaking, the photonic crystal transitioned from C_4^z symmetry to C_2^z symmetry (see Appendix D for further details). As a result, the degeneracy was broken, resulting in two bandgaps, as indicated by the gray dotted lines in the right panel of Fig. 2(a).

The modes supported by this structure were analyzed by considering those supported by a square array of two-dimensional YIG pillars. As depicted in Figs. 2(b)–2(d), this structure supported three modes for TM polarization near the 9 GHz frequency—a monopole mode, a transverse magnetic dipole mode, and a longitudinal magnetic dipole mode. When a magnetic field was applied, as illustrated in the right part of the panel, these three modes were displaced to different frequencies (8.95 GHz, 9.52 GHz, 11.04 GHz, respectively). Because of the broken TRS, all three modes were required to be rotated through 180° to coincide with each other.

We further calculated the Chern number of each photonic band from low frequency to high frequency near the Dirac point to be 0, 1, and −1, respectively. Based on the Chern number of each band, we calculated the Chern numbers of the bandgaps, 1 and 2 [right panel of Fig. 2(a)], to be $\Delta C_{\Gamma 1-2} = |C_{\Gamma 1}| = 0$ and $\Delta C_{\Gamma 2-3} = |C_{\Gamma 1} + C_{\Gamma 2}| = 1$, respectively. Based on the Chern numbers of the bandgaps, 1 and 2, we can determine their topological nature—bandgaps 1 and 2 were topologically trivial and nontrivial, respectively. Depending on

the Chern numbers of the bandgap, a topological nontrivial bandgap (10.24–11.04 GHz) near the Dirac point could be realized. This resulted in edge states localized at interfaces that were topologically protected. Being topologically protected, these edge states were immune to disorder and perturbations.

We experimentally characterized this metamaterial using the setup proposed by Zhou *et al.* [56]. The sizes of all the samples were designed to be 10 × 10 periods, as illustrated in Fig. 1(a). The parallel-plate waveguide consisting of two copper clad laminates separated by 4 mm supported only the fundamental transverse electromagnetic (TEM) mode in a parallel-plate waveguide below 37.5 GHz. To facilitate the excitation and measurement of electromagnetic fields inside the waveguide, a square array of holes, with a lattice constant of 5 mm, was drilled through the top surface of the copper clad laminate, enabling the insertion of a probe for field measurement. The thickness of the copper clad laminates was taken to be 2 mm to tune the uniform distribution of the magnetic flux.

First, we measured the photonic band structure of the metamaterial under an applied magnetic field of 0, as illustrated using the intensity plot in the left panel of Fig. 2(a). The band structure of the TM bulk states was obtained by applying two-dimensional discrete Fourier transform (2D-DFT) to the measured complex field distribution over the metamaterial (see Appendices A and E for further details). The measured photonic band structure exhibited good agreement with the
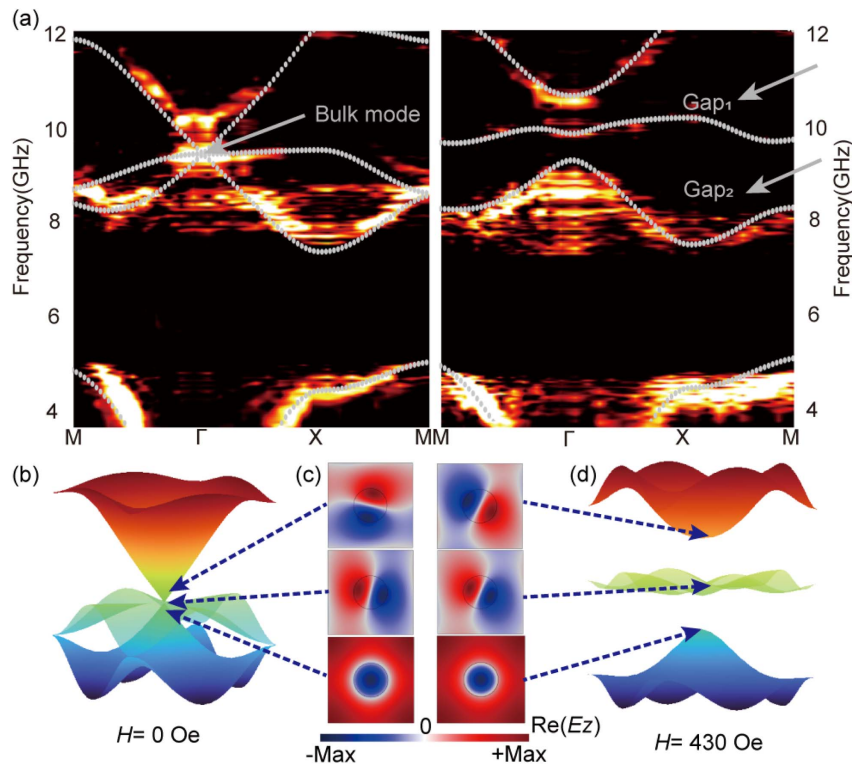

Fig. 2. Theoretical and experimental demonstration of an active ZIM. (a) Measured and calculated (gray dots) photonic bands of the active ZIM using Fourier transform field scan (FTFS) of the TM modes corresponding to applied magnetic fields of 0 (left panel) and 430 Oe (right panel). (b), (c) Simulated three-dimensional dispersion surfaces near the Dirac-point frequency, depicting the relationship between the frequency and the wave vectors (k_x and k_y). (d) COMSOL-computed Re(E_z) on the cross section of a ZIM unit cell at the frequencies indicated by dashed arrows, depicting an electric monopole mode, a transverse magnetic dipole mode, and a longitudinal magnetic dipole. The black circles indicate the boundaries of the YIG pillars.

simulation results (represented by gray dots). Both the measured and computed band structures exhibited a bandgap between 5 and 7 GHz as well as bulk modes between 7 and 12 GHz, indicating a Dirac-like cone dispersion near 9 GHz. The nondegeneracy of the photonic bands was also recorded after applying a 430 Oe magnetic field along the z direction, as depicted in the right panel in Fig. 2(a). The bandgaps were experimentally measured to be at 8.95–9.60 GHz and 10.24–11.04 GHz, corroborating the simulation results.

C. Phase Transition and Parameters Retrieval

The magnetic field-induced band structure and transmittance modulation can be regarded to be a phase transition process from a material perspective. This phenomenon can be observed by retrieving the effective permittivity and permeability tensor elements of the metamaterial in the presence and absence of an applied magnetic field, as illustrated in Fig. 3. We used the boundary effective medium approach (BEMA) to calculate the effective constitutive parameters, as proposed in a previous study on ZIM [57]. In Figs. 3(a)–3(c), ε_{eff} denotes the effective permittivity, μ denotes the diagonal of the effective permeability tensor, and κ denotes the off-diagonal component of the effective permeability tensor, $\begin{pmatrix} \mu & i\kappa & 0 \\ -i\kappa & \mu & 0 \\ 0 & 0 & 1 \end{pmatrix}$.

Figure 3(a) depicts the results corresponding to an applied magnetic field of 0. The real parts of ε_{eff} and μ cross zero simultaneously and linearly at 9 GHz, exhibiting ε-and-μ-near-zero behavior corresponding to the zero-index phase. The imaginary parts of ε_{eff} and μ were both close to 0. This low loss was attributed to the small loss tangent (0.0002) of the YIG material in this frequency range. When a magnetic field of 430 Oe was applied, phase transitions occurred from the zero-index phase to the μ-negative (MNG) or the ε-negative (ENG) phase, as depicted in Fig. 3(b) and Fig. 3(c), respectively. In the bandgap 8.95–9.6 GHz [Fig. 3(b)], ε_{eff} is positive, whereas μ_{eff} ($\mu_{\text{eff}} = \frac{\mu^2 - \kappa^2}{\mu}$) [41] is negative, which corresponds to the MNG phase. The impedance at 9 GHz was tuned from $1.84i$ to $0.62i$ after applying the magnetic field, leading to a total reflection of the incident electromagnetic (EM) wave owing to impedance mismatch. In the bandgap 10.24–11.04 GHz [Fig. 3(c)], ε_{eff} is negative, whereas μ_{eff} is positive, which corresponds to the ENG phase. Corresponding to both frequency

ranges, the real parts of ε_{eff} and μ_{eff} decreased as the frequency increased, exhibiting anomalous dispersion. The incident EM wave was still reflected due to impedance mismatch. Additionally, as depicted in the inset of Fig. 3(c) in the ENG frequency regime, a nontrivial topological boundary state was observed at the metamaterial edge because of the difference between the Chern numbers of the upper and lower structures.

The complex phase transition phenomena discussed above were attributed to the location of the ZIM at the origin of the metamaterial phase diagram, which allowed it to reach all quadrants of the phase diagram via appropriate tuning of the constitutive parameters [41,58]. Further discussion on the attainment of other phases based on the phase diagram is depicted in Figs. 9–11 of Appendices F and G. Such unique properties of an active ZIM are indicative of its potential with respect to the modulation of the propagation of EM waves.

D. Wave Propagation in Magnetically Tunable Zero-Index Metamaterials

To showcase a microwave switch based on the phase transition effect of active ZIM, we fabricated a ZIM waveguide switch by leveraging the contingency of the supercoupling state on the applied magnetic field, as illustrated in Fig. 4(a). First, a ZIM waveguide comprising top and bottom metal plates and 100 YIG pillars was fabricated, forming two sharp 90-deg bends, to verify the supercoupling effect experimentally (see Appendices A and H for further details). The waveguide was coupled to the coaxial line via sub-miniature version A (SMA) connectors. Linear tapered sections were used to sustain the TE_{10} mode and induce its gradual evolution into the TM mode of the metamaterial during propagation from the source to the waveguide. Perfect magnetic conductor (PMC) boundary conditions were realized using aluminum alloy walls at a distance of $\lambda/4$ from the metamaterial as the lateral boundaries [30] (see Appendices A and H for further details). Using the device depicted in Fig. 4(a), we successfully switched between the bulk state (supercoupling state) and the photonic bandgap state (off state) by applying appropriate magnetic fields to the YIG pillars.

Figure 4(b) depicts the measured transmission spectra corresponding to both states. A large transmission contrast was observed over 8.9–9.4 GHz, which was consistent with the bandgap frequencies calculated via numerical simulation in
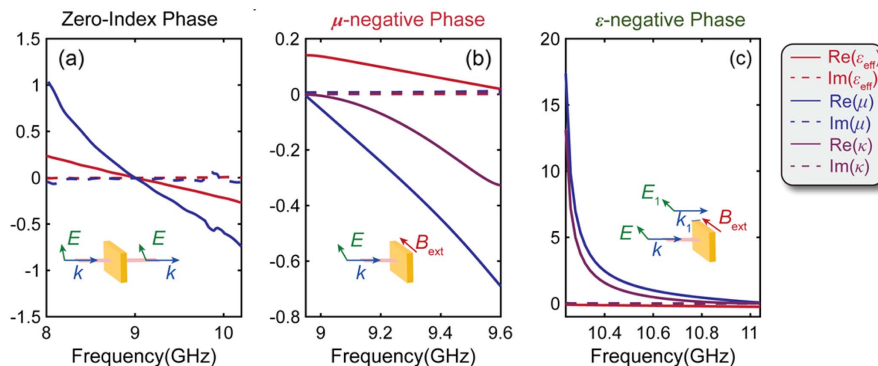

Fig. 3. Magnetic field-induced phase transition of active ZIM. Real and imaginary parts of the effective permittivity (ε_{eff}) and permeability tensor elements (μ and κ) (a) under an applied magnetic field of 0, and under an applied magnetic field of 430 Oe in (b) the bandgap frequency range of 8.95–9.60 GHz and (c) the bandgap frequency range of 10.24–11.04 GHz.
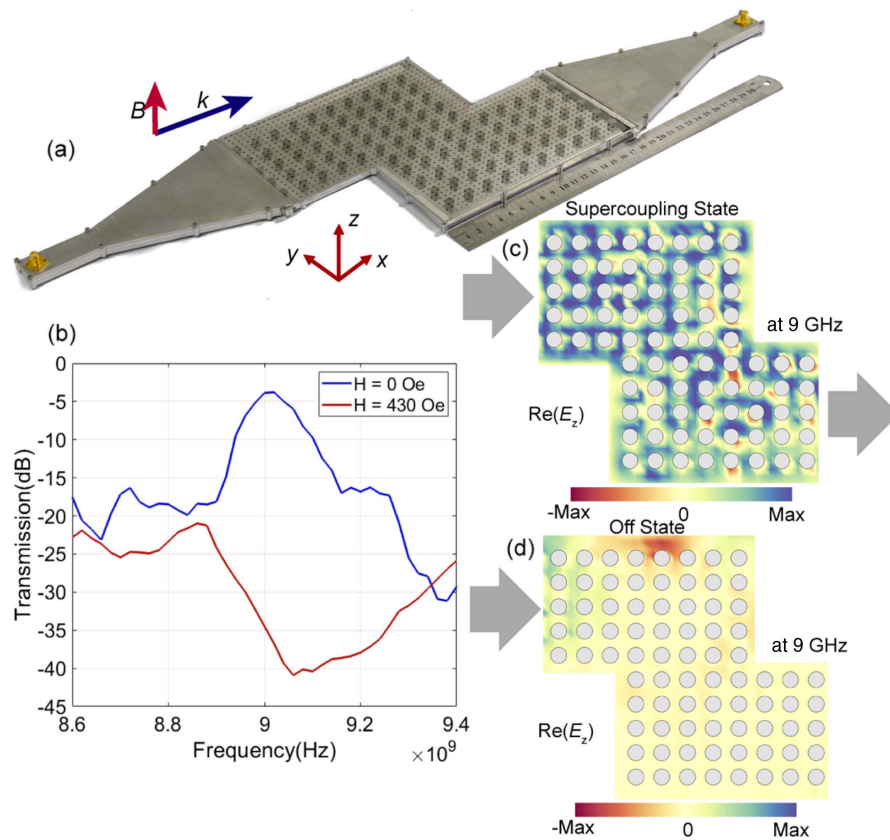
Fig. 4. Structure and characterization of a microwave switch based on active DCZIM. (a) Photograph of the microwave switch sample. (b) The measured transmissions in the absence and presence of an applied magnetic field of 430 Oe. (c) The real part of the E_z distribution observed at 9 GHz inside the metamaterial (each pillar is indicated in gray) in the absence of a magnetic field. (d) The real part of the E_z distribution observed at 9 GHz inside the metamaterial (each pillar is indicated in gray) in the presence of a 430 Oe magnetic field.

Fig. 2(a). The difference in device transmission under zero and 430 Oe magnetic fields was larger than 30 dB at approximately 9 GHz and the device insertion loss was 3.75 dB. Considering that the coupling loss induced by the SMA connectors was 2.8 dB, the intrinsic loss of the ZIM waveguide was as low as 0.95 dB, primarily induced by the absorption of YIG materials. Notably, such on–off switching effect can also be observed as a giant Cotton–Mouton effect due to the zero-index property, which was not observed in conventional ferrite-based waveguide devices. A much larger extinction ratio up to 104 dB can be achieved by simply making a longer device (see Appendix J). Such devices may show fast switching speed of kilohertz to megahertz similar to conventional ferrite switches, but also show higher extinction ratio and smaller device footprint, making them particularly attractive for microwave switch applications.

We verified the supercoupling behavior in the absence of an applied magnetic field by measuring the E_z component of the electric field at each point of the metamaterial, as illustrated in Fig. 4(c). At 9 GHz, the electric field tunneled through the metamaterial with almost no phase change in the form of a bulk mode, verifying supercoupling behavior. In contrast, in the absence of YIG pillars in the waveguide, the wave was reflected back to the incident port, as described in Appendix H. This confirmed that the supercoupling behavior was induced by

the DCZIM. As depicted in Fig. 4(d), in the presence of an applied magnetic field, the electromagnetic wave decayed exponentially in the metamaterial owing to the photonic bandgap 1 depicted in Fig. 2(a), leading to a high extinction ratio. We also constructed a switch between the supercoupling state and the topological one-way transmission state by probing at the upper bandgap frequency of 10.6 GHz (see Appendix I for further details). This property can be used to fabricate efficient non-reciprocal phase shifters with compact device size. These unique properties are indicative of the potential of active ZIMs in novel active electromagnetic devices.

3. CONCLUSION

In this study, we proposed and experimentally operated a magnetically tunable ZIM. The metamaterial was operated by leveraging the Cotton–Mouton effect of the constitutive YIG pillars under applied magnetic fields, which alter the symmetry and bandgap opening of the Dirac-like cone-based ZIM. Such a ZIM shows an effective refractive index near zero ($|n_{\text{eff}}| < 0.1$) over a bandwidth of 6.77% in the absence of an applied magnetic field, and 5.43% (extinction ratio over 100 dB) when applying magnetic field, which means the bandwidth of our device is comparable with the commercial device. From a material perspective, the proposed metamaterial exhibited a

phase transition from the zero-index phase to a single negative phase, leading to an effective index change from 0 to 0.09i at 9 GHz. Based on this property, we constructed and verified the function of a microwave switch by manipulating the supercoupling effect, thereby reducing the intrinsic loss to 0.95 dB and achieving a high extinction ratio of 30.63 dB at 9 GHz.

We believe that this study introduces a new approach to active ZIMs, particularly with respect to the development of efficient active electromagnetic and nonreciprocal devices. Utilizing the giant Cotton–Mouton effect, efficient ferrite switches with large extinction ratio and compact device size can be fabricated. Compact and efficient ferrite phase shifters can be fabricated based on the phase transition from the supercoupling state to the topological boundary state. By appropriately engineering the slots in parallel-plate copper waveguides [31], continuous beam steering over the broadside can be achieved by varying the applied magnetic field. Moreover, our design can be extended to the optical regime by embedding YIG pillars in a polymer matrix with gold films cladded [26], enabling the dynamic modulation of optical DCZIM. Further, such a magnetically tunable DCZIM can be used to modulate the four-wave mixing process in DCZIM by manipulating the zero-index phase-matching condition [10]. Additionally, we were able to modulate DCZIM-based large-area single-mode photonic crystal surface-emitting lasers with high output power [59]. Finally, we also successfully modulated the extended superradiance by tuning the effective index of the DCZIM, in which many quantum emitters were embedded [12].

APPENDIX A: METHODS

1. Numerical Simulation

The permittivity of the YIG used during numerical simulation was taken from that published by Zhou _et al._ [60]. The band structure was calculated using the COMSOL software. The results were obtained by calculating the modes with periodic boundary conditions along the x and y directions. The TM polarization mode was selected by considering the electric field to be an out-of-plane vector. Under magnetic fields, the DCZIM was simulated to obtain frequency-dependent electromagnetic field profiles. The transitions between the different metamaterial phases in the presence and absence of magnetic fields were simulated by considering the off-diagonal elements of the YIG permeability tensor. Home-made MATLAB codes based on BEMA and 2D-DFT were used to calculate the effective permittivity, permeability tensor, and photonic band structure.

2. Device Fabrication

The active DCZIM consisted of a square array of YIG pillars with a radius of 3.53 mm, a height of 4 mm, and a lattice constant of 17.9 mm [as indicated in Fig. 1(a)]. The waveguide was formed using two 500 mm × 500 mm copper clad laminates. During the measurement of the nontrivial boundary state, a copper bar with a length of 40 cm and a width of 2 cm was placed at the edge of the metamaterial to form its boundary.

The YIG pillars were fabricated from YIG bulk crystals using an ultra-high-accuracy computer numerical control (CNC)

machine (Mazak VARIAXIS i-700) with a dimensional accuracy exceeding 0.05 mm. As depicted in Fig. 1(a), an external magnetic field was introduced to maintain the saturation magnetization of the garnet. To affix the YIG pillars to the copper clad laminate substrate tightly, double-sided tape with a radius of 3.53 mm was applied to one side of each pillar. The position of each YIG pillar was precisely defined by placing the other side in an acrylic mold with 10 × 10 holes with a radius of 3.54 mm and a lattice constant of 17.9 mm. The copper clad laminate substrate was pressed onto the side of the YIG pillars with tape, which affixed the YIG pillars tightly and precisely onto the copper clad laminate substrate. The acrylic mold was removed carefully to prevent extrusion and damage to the YIG pillars.

Each YIG pillar was properly magnetized by aligning the NdFeB magnet used to apply the magnetic field precisely underneath each YIG pillar. To this end, a 2 mm thick acrylic sheet was first covered with a double-sided tape to form the substrate. Then, we fixed a 5 mm thick acrylic sheet including 10 × 10 perforations with a radius of 5 mm and a lattice constant of 17.9 mm onto a 2 mm thick acrylic substrate. Finally, with respect to the designated direction of the magnetic field, we placed the NdFeB magnets into the holes of the 5 mm thick acrylic sheet, achieving a good alignment with the array of the YIG pillars [Fig. 1(b)].

3. Characterization Setup

We measured the photonic band structure, transmission spectra, and near-field distribution of the active metamaterial sample using two dipole antennas as the transmitter and receiver. Both antennas were inserted into the waveguide via holes drilled using an ultra-high-precision CNC machine and they were connected to a vector network analyzer (Rohde & Schwarz ZNB 20) to measure the S parameters. Prior to measurement, 3.5 mm 85052D through-open-short-load calibrations were performed. As a result, the measured S parameters included only the insertion loss of the tapered waveguides and the metamaterial.

APPENDIX B: THE COTTON–MOUTON EFFECT OF YIG

When biased by a magnetic field along the z axis ($H_{\text{ext}} \| z$), the magnetic permeability of YIG is given by the following:

$$
\tilde{\mu} = \mu_0 \begin{pmatrix} \text{Re}(\mu_{\text{YIG}}) - i\text{Im}(\mu_{\text{YIG}}) & i(\text{Re}(\kappa_{\text{YIG}}) - i\text{Im}(\kappa_{\text{YIG}})) & 0 \\ -i(\text{Re}(\kappa_{\text{YIG}}) - i\text{Im}(\kappa_{\text{YIG}})) & \text{Re}(\mu_{\text{YIG}}) - i\text{Im}(\mu_{\text{YIG}}) & 0 \\ 0 & 0 & 1 \end{pmatrix}
$$

$$
= \begin{pmatrix} \mu_{\text{YIG}} & i\kappa_{\text{YIG}} & 0 \\ -i\kappa_{\text{YIG}} & \mu_{\text{YIG}} & 0 \\ 0 & 0 & 1 \end{pmatrix}, \tag{B1}
$$

$$
\begin{cases} \nabla \cdot (\varepsilon_{\text{YIG}} E) = 0 \\ \nabla \times E = -i\omega\tilde{\mu}_{\text{YIG}} H \\ \nabla \cdot (\tilde{\mu}_{\text{YIG}} H) = 0 \\ \nabla \times H = i\omega\varepsilon_{\text{YIG}} E \end{cases}. \tag{B2}
$$

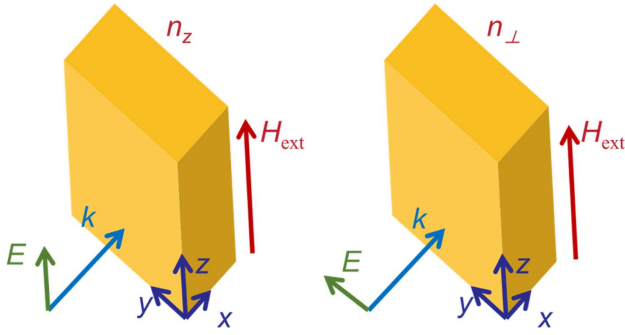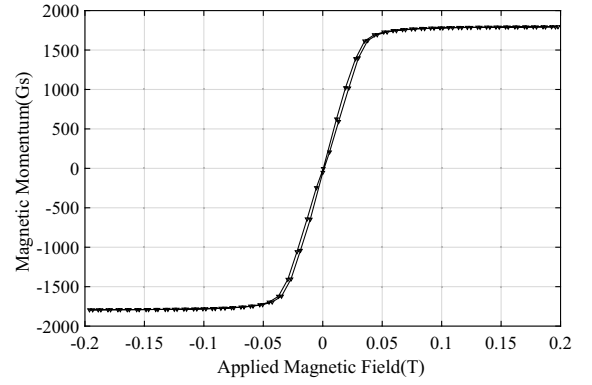**Fig. 5.** Schematic diagram depicting the Cotton–Mouton effect.

Fig. 6. Magnetic hysteresis loop of a YIG pillar measured using a vibrating sample magnetometer (VSM) at room temperature (300 K). The sample was magnetically saturated under a small applied magnetic field of ~0.04 T, with negligible remanence of ~10 Gauss and saturation magnetization of 1780 Gauss.

For TM-polarized plane waves, the only nonzero component of the electric field ($E \| H_{ext}$) is the z component ($E_x = 0$, $E_y = 0$, $E_z \neq 0$). Assuming that the wave vector k lies along the x axis, the Helmholtz equation becomes

$$\nabla \times (\nabla \times E) - \omega^2 \varepsilon_{YIG} \tilde{\mu}_{YIG} E = 0. \qquad \text{(B3)}$$

We can simplify the above equation as follows:

$$-\nabla^2 E_z = i\omega(\mu_{YIG}(\partial x H_y - \partial y H_x) - i\kappa_{YIG}(\partial x H_x + \partial y H_y)). \qquad \text{(B4)}$$

Because of the third term in Maxwell's equations, $\nabla \cdot (\tilde{\mu}_{YIG} H) = 0$,

$$-i\kappa_{YIG}(\partial x H_y - \partial y H_x) = \mu_{YIG}(\partial x H_x + \partial y H_y). \qquad \text{(B5)}$$

Therefore, we obtain

$$\left(\nabla^2 + \varepsilon_{YIG} \left(\frac{\mu_{YIG}^2 - \kappa_{YIG}^2}{\mu_{YIG}} \right) \omega^2 \right) E_z = 0. \qquad \text{(B6)}$$

Comparing this equation with the equation $\nabla \times (\nabla \times E) - \omega^2 \varepsilon_{YIG} \tilde{\mu}_{YIG} E = 0$, we obtain the effective refractive index:

$$n_z = \sqrt{\varepsilon_{YIG} \left(\frac{\mu_{YIG}^2 - \kappa_{YIG}^2}{\mu_{YIG}} \right)}. \qquad \text{(B7)}$$

Following the above derivation, the effective index of the TE mode is given by

$$n_\perp = \sqrt{\varepsilon_{YIG} \mu_{YIG}}. \qquad \text{(B8)}$$

The above analysis demonstrates that, in the case of linear polarization, the effective refractive index of YIG is modulated by material magnetization—namely the Cotton–Mouton effect, as shown in Fig. 5.

APPENDIX C: THE PERMITTIVITY, PERMEABILITY, AND ROOM TEMPERATURE MAGNETIZATION HYSTERESIS OF YIG

At the frequency studied, YIG is an isotropic material with a relative permittivity of 13 and a dielectric loss tangent of 0.0002 [60]. The saturation magnetization was measured to be $4\pi M_s = 1780$ Gauss, as shown in Fig. 6, and the ferromagnetic resonance linewidth was 35 Oe. When biased by an applied magnetic field along the z axis, the magnetic permeability of the YIG pillars has the form of Eq. (B1), where

$$\text{Re}(\mu_{YIG}) = 1 + \frac{\omega_0 \omega_m (\omega_0^2 - \omega^2) + \omega_0 \omega_m \omega^2 \alpha^2}{((\omega_0^2 - \omega^2(1+\alpha^2)))^2 + 4\omega_0^2 \omega^2 \alpha^2}, \qquad \text{(C1)}$$

$$\text{Im}(\mu_{YIG}) = \frac{\alpha \omega_0 \omega_m ((\omega_0^2 + \omega^2(1+\alpha^2)))^2}{((\omega_0^2 - \omega^2(1+\alpha^2)))^2 + 4\omega_0^2 \omega^2 \alpha^2}, \qquad \text{(C2)}$$

$$\text{Re}(\kappa_{YIG}) = \frac{\omega_0 \omega_m ((\omega_0^2 - \omega^2(1+\alpha^2)))^2}{((\omega_0^2 - \omega^2(1+\alpha^2)))^2 + 4\omega_0^2 \omega^2 \alpha^2}, \qquad \text{(C3)}$$

$$\text{Im}(\kappa_{YIG}) = \frac{2\omega_0 \omega_m \omega^2 \alpha}{((\omega_0^2 - \omega^2(1+\alpha^2)))^2 + 4\omega_0^2 \omega^2 \alpha^2}. \qquad \text{(C4)}$$

$\omega_0 = \gamma \mu_0 M_s$, $\omega_m = \gamma \mu_0 H_z$, $\alpha = 0.0088$ denotes the damping coefficient, and ω denotes the operating frequency [61].

In accordance with the aforementioned model, when a magnetic field of 430 Oe was applied, the ferromagnetic resonance frequency of YIG was 1.20 GHz. The real and imaginary parts of the permeability tensor of the material with respect to the frequency are depicted in Fig. 7.

APPENDIX D: SYMMETRY ANALYSIS OF THE DCZIM

As described using topological theory and group theory, the "Dirac points" are protected by "PT-symmetry" in the entire Brillion zone, in which P indicates the parity inversion and T indicates the time-reversal symmetry [62]. Therefore, when a zero magnetic field is applied, the proposed DCZIM structure preserved C_4^z symmetry (i.e., 90-deg rotation symmetry around the axis) at the Γ point, resulting in the following mode profile of the system:

$$H(x, y, z) = H(y, -x, z) = H(-x, -y, z). \qquad \text{(D1)}$$

When a magnetic field along the z axis was applied, time-reversal symmetry was broken, as was the product of time-reversal symmetry (T) and parity (P) inversion. As a result, the Dirac cones opened and the degeneracy was lifted, i.e.,
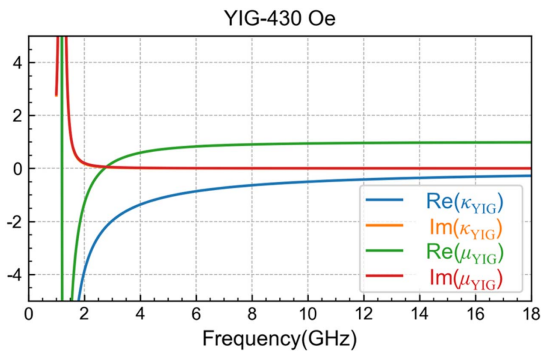
Fig. 7. Real and imaginary parts of the permeability tensor of YIG under the applied 430 Oe magnetic field.

$$H(x, y, z) \neq H(-x, -y, z). \tag{D2}$$

However, the following part of C_4^z symmetry still remained valid:

$$H(-x, -y, z) = H(y, -x, z). \tag{D3}$$

Therefore, when the DCZIM structure preserves C_4^z symmetry under a T-breaking operation, only C_2^z symmetry is retained. This proves that the magnetized DCZIM exhibits symmetry variation from C_4^z to C_2^z.

APPENDIX E: CHARACTERIZATION OF THE PHOTONIC BAND STRUCTURE USING THE FTFS METHOD

We characterized the photonic band structure of the DCZIM using Fourier transform field scan (FTFS) measurements—the results are depicted in Figs. 8(a)–8(d) [63,64]. As the maximum resolution of a Brillouin zone is determined by the number of real-space unit cells in each direction, the first Brillouin zone is denoted by the square region in Fig. 8(b), where the field was excited by placing the source at each corner of the sample and measured across the sample. The fields were stitched together as illustrated in Fig. 8(a). In the magnetized DCZIM, the symmetry of the photonic crystal was reduced to C_2^z. In this case, the resolution could also be increased by inverting the measured field profiles along the x or y direction.

APPENDIX F: PHOTONIC BAND STRUCTURES OF THE DCZIM UNDER DIFFERENT APPLIED MAGNETIC FIELDS

We simulated the photonic band structures of the DCZIM under different applied magnetic fields, as illustrated in Figs. 9(a) and 9(b). As depicted in Fig. 9(a), as the magnetic field was increased, the photonic bands gradually shifted to
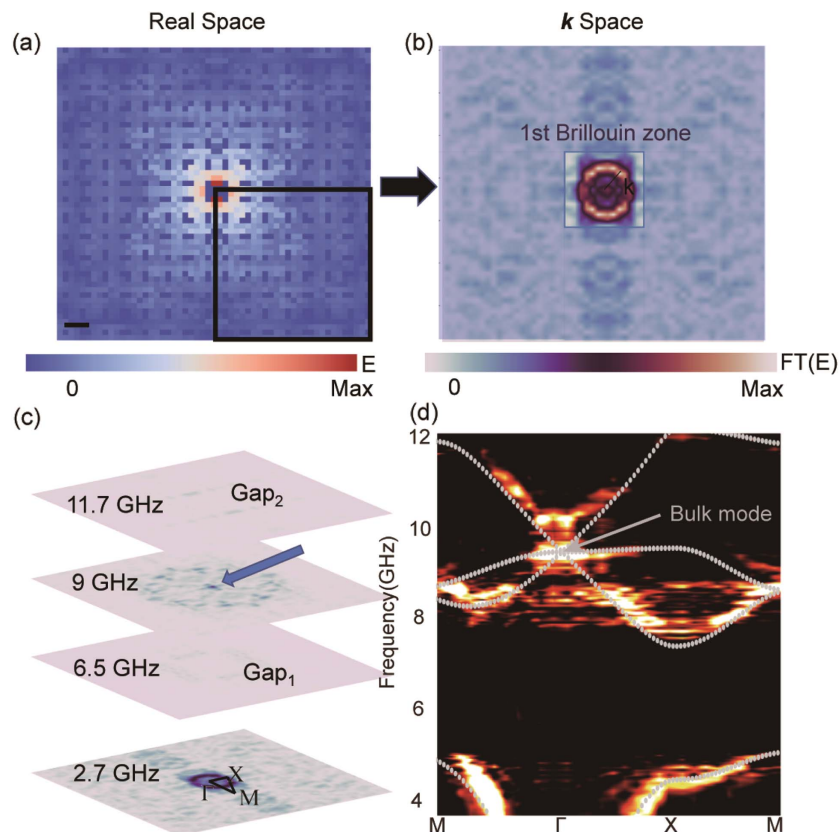

Fig. 8. Measurement of the photonic band structure via FTFS. (a) Electric fields measured across the photonic crystal at 2.70 GHz. The source was placed at one corner of the sample, and the field was measured across the sample. Owing to the C_4^z symmetry of the photonic crystal, fields in the other three quadrants could be obtained based on symmetry considerations. The fields were then stitched together to obtain a larger effective sampling area. (b) Field intensity in the reciprocal lattice space obtained via Fourier transform of (a). The first Brillouin zone is denoted by the square region. (c) Isofrequency contours of the Brillouin zone at different frequencies. (d) The 2D photonic band structure of the DCZIM structure. The FTFS data corresponding to high-symmetry points were obtained via interpolation.
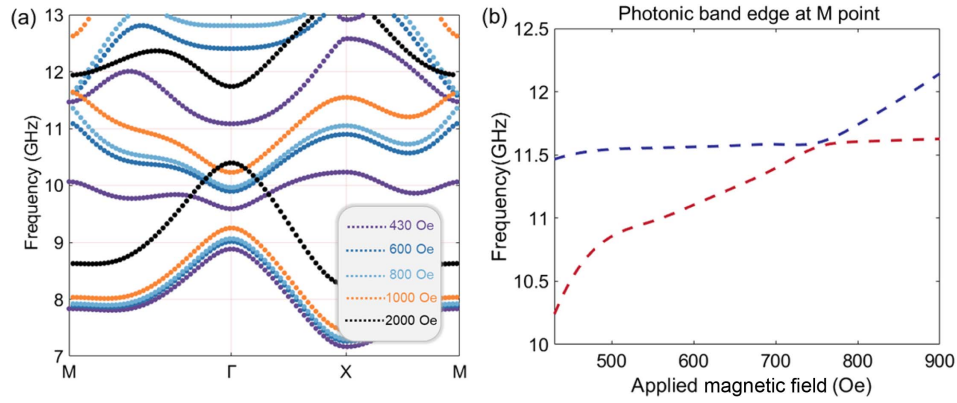
Fig. 9. (a) Simulated band structures of the DCZIM under different applied magnetic fields. (b) The band edges of the bandgap, 10.24–11.04 GHz, at M as a function of the applied magnetic field.

higher frequencies. The photonic bandgap 8.95–9.60 GHz (corresponding to the 430 Oe field) exhibited similar bandgap widths under different applied magnetic fields. On the other hand, the bandgap 10.24–11.04 GHz (corresponding to the 430 Oe field), first closed and then opened as the magnetic field was increased. This was observed by plotting the band edges at the point M, as depicted in Fig. 9(b).

APPENDIX G: EFFECTIVE CONSTITUTIVE PARAMETERS AND PHASE TRANSITION OF THE DCZIM UNDER DIFFERENT APPLIED MAGNETIC FIELDS

We simulated the effective constitutive parameters of the DCZIM as a function of the applied magnetic field using the theory proposed by Wang *et al.* [57], as illustrated in Fig. 9. Using BEMA [57], the effective electric displacement and magnetic fields were calculated based on the line integral of the numerically simulated eigenmode fields along the x and y directions. Using the constitutive relationship, the following formula was obtained:

$$\begin{pmatrix} D_z(k_x) \\ D_z(k_y) \end{pmatrix} = \varepsilon_0 \varepsilon_{\text{eff}} \begin{pmatrix} E_z(k_x) \\ E_z(k_y) \end{pmatrix}, \quad \textbf{(G1)}$$

where ε_{eff} denotes the effective permittivity of the metamaterial, and $D_z(k_x)$, $D_z(k_y)$, $E_z(k_x)$, and $E_z(k_y)$ denote the z-direction components of the effective electric displacement and effective electric field along the x and y directions, respectively. Similarly, the relationship between B and H is given by

$$\begin{pmatrix} B_x(k_x) & B_x(k_y) \\ B_y(k_x) & B_y(k_y) \end{pmatrix} = \mu_0 \begin{pmatrix} \mu & i\kappa \\ -i\kappa & \mu \end{pmatrix} \begin{pmatrix} H_x(k_x) & H_x(k_y) \\ H_y(k_x) & H_y(k_y) \end{pmatrix}, \quad \textbf{(G2)}$$

where $B_x(k_x)$, $B_x(k_y)$, $H_x(k_x)$, and $H_x(k_y)$ denote the x-direction components of the effective magnetic flux density and effective magnetic field along the x and y directions, respectively, and $B_x(k_x)$, $B_x(k_y)$, $H_x(k_x)$, and $H_x(k_y)$ denote the y-direction components of the effective magnetic flux density and effective magnetic field along the x and y directions, respectively.

Using the aforementioned methods, we obtained the effective permittivity and permeability tensors of metamaterials under different applied magnetic fields. The cases in which the magnetic field was increased to 600–800 Oe are depicted in Fig. 10. Figures 10(a) and 10(c) present the real parts of ε_{eff} and μ corresponding to the frequency ranges 9.08–9.89 GHz for the 600 Oe field and 9.18–10.03 GHz for the 800 Oe field (corresponding to the lower bandgaps in Fig. 9). The real part of ε_{eff} was positive, whereas the real part of μ_{eff} ($\mu_{\text{eff}} = \frac{\mu^2 - \kappa^2}{\mu}$) was negative ($\mu$ was negative, κ was negative, and the absolute value of κ was less than μ) in the MNG phase. Corresponding to the aforementioned frequency ranges, the real parts of ε_{eff} and μ_{eff} decreased with an increase in frequency. The incident EM wave was reflected owing to impedance mismatch.

Figures 10(b) and 10(d) present the effective constitutive parameters corresponding to the frequency ranges 11.28–11.64 GHz for the 600 Oe field and 11.55–11.79 GHz for the 800 Oe field (corresponding to the upper bandgaps). The real part of ε_{eff} was negative, whereas that of μ_{eff} was positive in this case. μ was negative, but the absolute value of κ's real part was larger than that of μ, which made the real part of μ_{eff} ($\mu_{\text{eff}} = \frac{\mu^2 - \kappa^2}{\mu}$) positive, leading to high reflection from the metamaterial. The opacity of the metamaterial was induced by the gyromagnetic properties, κ, of YIG. In the theoretical proposal by Davoyan *et al.* [41], such a magnetic-field-induced low-transmittance state was called "Hall opacity."

The aforementioned modulation of the effective constitutive parameters is plotted in a metamaterial phase diagram in Fig. 11. The phase of the metamaterial was determined by ε_{eff}, μ, and the gyromagnetic properties, κ. We illustrate the cases corresponding to applied magnetic fields of 0, 430 Oe, and 600 Oe. When a zero magnetic field was applied, the active DCZIM at 9 GHz was in a zero-index phase at the origin of the phase diagram. When a 430 Oe magnetic field was applied, the phase of the metamaterial changed to MNG corresponding to the frequency range 8.95–9.60 GHz, and to ENG corresponding to the frequency range 10.24–11.04 GHz, as indicated by the stars in the figure. When a 600 Oe magnetic field was applied, the phase of the metamaterial changed to MNG corresponding to the frequency range 9.08–9.89 GHz,
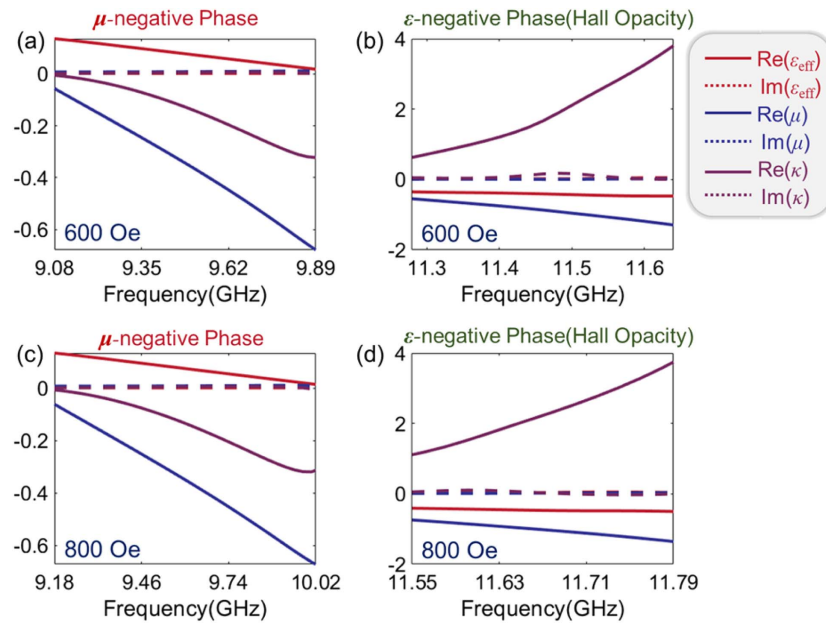
Fig. 10. Effective constitutive parameters of the DCZIM under (a), (b) 600 Oe field and (c), (d) 800 Oe field, as calculated using BEMA.
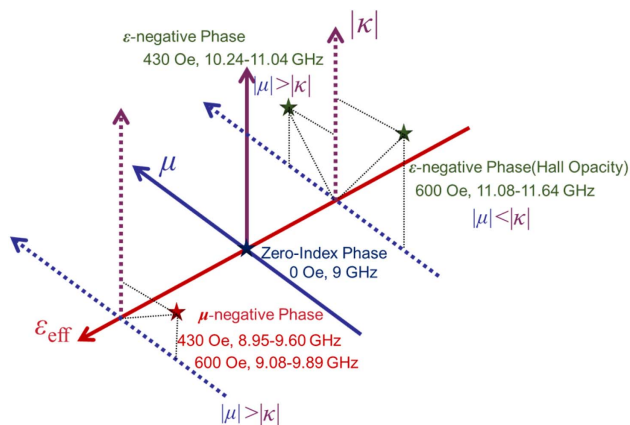

Fig. 11. Magnetic field-induced phase transition of active DCZIM under different applied magnetic fields.

Fig. 12. Device structure of the microwave switch.

whereas it changed to ENG with Hall opacity behavior corresponding to the frequency range 11.08–11.64 GHz. The complex phase transition process of DCZIM was essentially determined by its location at the origin, enabling the transition to any phase in the metamaterial phase diagram via proper modulation.

APPENDIX H: DEVICE STRUCTURE OF THE MICROWAVE SWITCH AND ELECTRIC FIELD AND PHASE MEASUREMENT OF THE 90-DEG BENT WAVEGUIDE WITHOUT YIG PILLARS

Figure 12 presents the detailed structure of the fabricated microwave switch. The entire device was constructed using #6061 aluminum alloy with a manufacturing accuracy of ±0.005 mm. Holes with a diameter of 2 mm and a period of 5 mm were drilled through the top aluminum alloy plate.
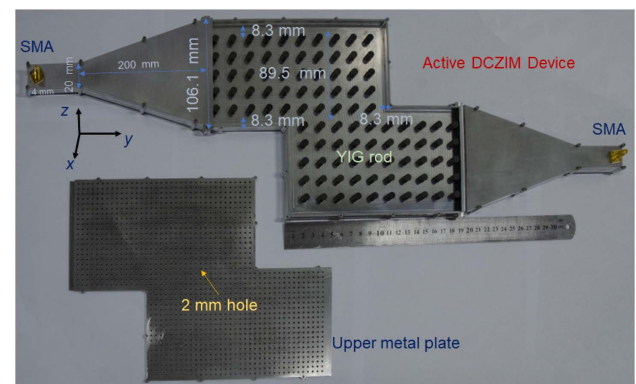
The width and height of the rectangular waveguide were 20 and 4 mm, respectively. The tapered waveguide sections were shaped like isosceles trapezoids on the *x-y* plane. The lengths of the two parallel sides of the isosceles trapezoid were 20 and 106.1 mm, respectively, the height of the isosceles trapezoid was 200 mm, and the height perpendicular to the propagation plane was 4 mm. Details of the tapered and bent waveguide geometries are depicted in Fig. 12. A PMC boundary condition was constructed by maintaining a distance of $\lambda/4$ (8.3 mm) between the aluminum alloy walls and photonic crystal boundary. In this case, the electric field parallel to the wall experienced a 90-deg phase advancement while propagating through the $\lambda/4$ gap, a 180-deg phase shift owing to the reflection from the perfect electric conductor (PEC), and finally another 90-deg phase advancement while propagating back through the $\lambda/4$ gap, leading to a total phase advance of 0, which is equivalent to a PMC boundary.

To verify that the supercoupling effect depicted in Fig. 4 was induced by the DCZIM, we measured the electric-field
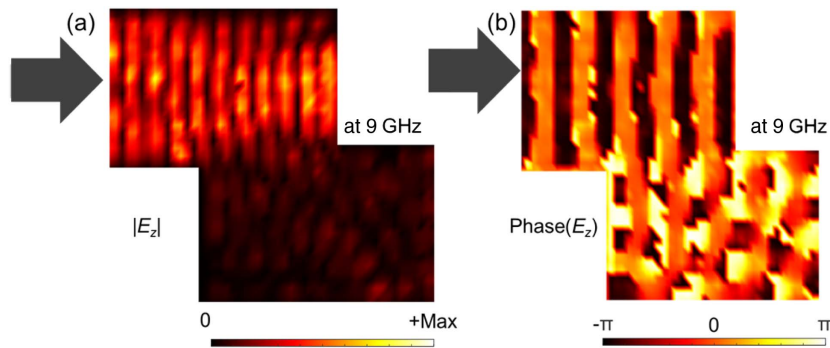
Fig. 13. (a) Electric field intensity and (b) phase distributions of 90 deg bent waveguide without YIG pillars.

intensity and phase distribution in a waveguide without YIG pillars. As illustrated in Fig. 13, following taper mode evolution, the TE_{10} mode gradually evolved into the TM mode, and the plane wave behavior was maintained until the metamaterial region was entered. However, the wave entering the metamaterial region was reflected by the 90 deg bend, leading to very low transmission through the exit port. In addition, the phase distribution within the metamaterial region was significantly distorted. These results demonstrate that the supercoupling effect illustrated in Fig. 4 was induced by DCZIM.

APPENDIX I: DEMONSTRATION OF A TOPOLOGICAL NONTRIVIAL BOUNDARY STATE IN MAGNETIZED DCZIM

As described in the main text, the Chern number of the bandgap 10.24–11.04 GHz, is 1 [Fig. 2(a)]. If a boundary is introduced into the active metamaterial, a topological

nontrivial boundary state is observed. This effect has been theoretically simulated and experimentally demonstrated. As depicted in Fig. 14(a), the sample was formed by adding a copper bar to the boundary of the metamaterial. A source antenna was placed at the boundary and a probe antenna was used to measure the transmittance and field distribution along the boundary. As depicted in Fig. 14(c), the difference between the forward and backward transmissions exceeded 50 dB at approximately 10.6 GHz, indicating the unidirectionality of the boundary states. Further, the nonreciprocal-transmission frequency window, 10.24–11.04 GHz, was consistent with the boundary state in the numerical simulation, as depicted in Fig. 14(b). Additionally, the field distribution at 10.6 GHz inside the sample was mapped point-by-point, as presented in Fig. 14(e). The electric fields were observed to be strongly confined to the boundary and capable of propagating robustly across two sharp 90 deg corners, without any backscattering. This result agrees with our theoretical prediction presented in Fig. 14(d),
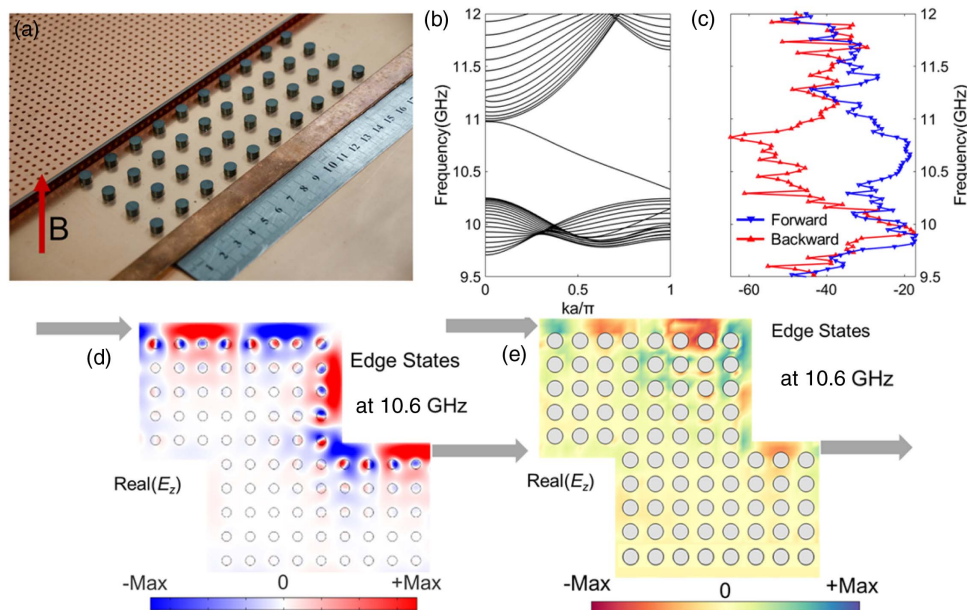

Fig. 14. Observation of topologically protected unidirectional boundary state in the metamaterial. (a) The structure of the active metamaterial sample with a boundary formed by a copper bar. (b) Numerically simulated projected band structure of the metamaterial with a strip with 20 unit cells in the y direction. (c) Transmission spectra measured by antennas located at the boundary. (d) Simulated real part of E_z field distribution at 10.6 GHz inside the sample [Fig. 4(a)] under a 430 Oe magnetic field. (e) The real part of the E_z field distribution measured at 10.6 GHz inside the sample [Fig. 4(a), each pillar represented in gray] under a 430 Oe magnetic field.
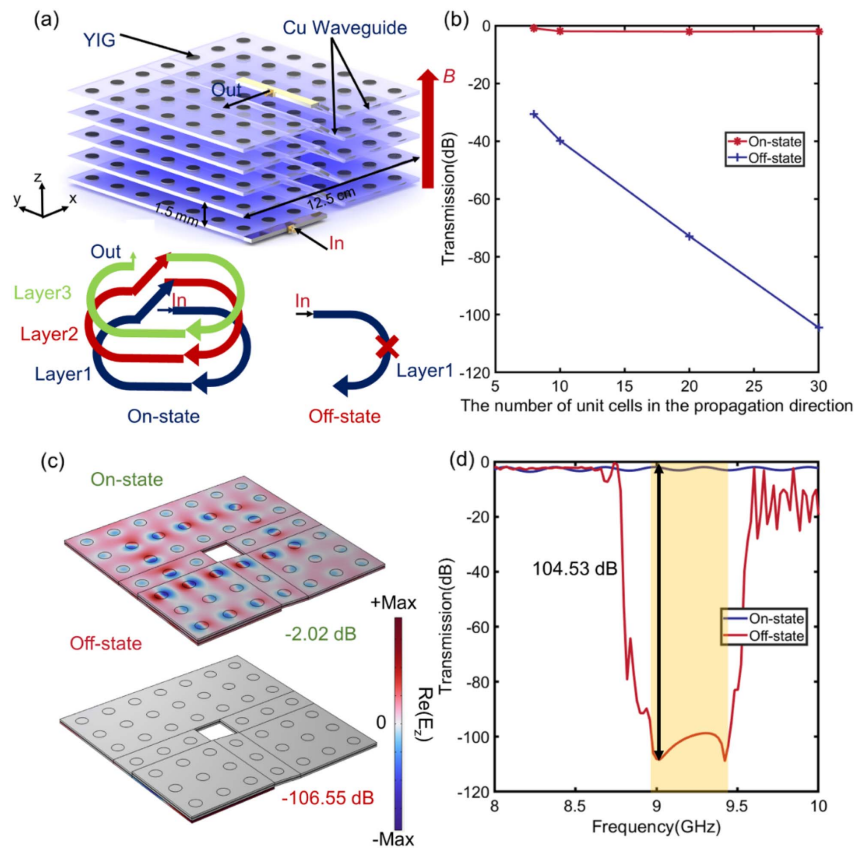
Fig. 15. Observation of a much larger extinction ratio in the ultra-compact spiral magnetically tunable ZIM switch staircase structure. (a) The structure of the spiral magnetically tunable ZIM switch staircase structure. Each layer in the structure is 1.5 mm high which contains 1 mm high metal waveguides and 0.5 mm interlayer air gaps. (b) Transmission spectra of the magnetically tunable ZIM switch's on state and off state. (c) The real part of the E_z field distribution at 9 GHz inside the sample. Upper panel: on state (without magnetic field applied) with –2.02 dB insertion loss. Lower panel: off state (with 430 Oe magnetic field applied) with –104.53 dB extinction ratio. (d) The simulated transmissions spectra of the proposed structure of Fig. 15 in the absence and presence of an applied magnetic field of 430 Oe.

confirming the existence of a topological nontrivial boundary state in the magnetized metamaterial.

APPENDIX J: DEMONSTRATION OF A MUCH LARGER EXTINCTION RATIO IN THE ULTRA-COMPACT MAGNETICALLY TUNABLE SPIRAL STAIRCASE ZIM SWITCH

As mentioned in the main text, the ZIM structure can support tunneling waveguides composed of arbitrary shapes because of its equivalent infinite wavelength. This novel feature of ZIM enables it to serve as one of the most suitable structures for switching. For magnetic ZIM-based RF switches, the extinction ratio can be enhanced by simply increasing the device length, whereas the insertion loss can be kept low due to the supercoupling effect. As depicted in Fig. 15(a), we proposed a new device design using a spiral staircase structure; each layer of the structure contains three unit cells perpendicular to the propagation direction (in plane). Two microstrip lines served as the source and probe antenna, and the magnetic field is applied in the z direction. As shown in Fig. 15(b), the simulated extinction ratio of this device exceeded 100 dB with approximately 25 unit cells in the propagation direction. While the

insertion loss is kept low at –2.02 dB. The field distribution of this device is shown in Fig. 15(c). When no magnetic field is applied, the structure is at the on state. The electromagnetic wave tunnels through the "in" port to the "out" port along the staircase, as shown in the left panel. Under a magnetic field of 430 Oe, the structure is switched to the off state, with almost no field intensity shown in the right panel. Undoubtedly, we can continue to increase the extinction ratio by increasing the length in the propagation direction of the device without significantly changing the insertion loss, while maintaining the device footprint. It should be noted that this device shows much higher extinction ratio (>100 dB) compared to conventional ferrite RF switches (~40 dB) using the Faraday effect [65]. Thanks to the supercoupling effect, the device footprint is only around 100 cm³, notably smaller than conventional RF switches (300–800 cm³) [65–67]. Meanwhile, an operation bandwidth (extinction ratio over 100 dB) up to 5.43% is observed, as shown in Fig. 15(d), comparable to conventional devices. These features make magnetic ZIMs promising for RF switch applications.

REFERENCES

1. I. Liberal and N. Engheta, "Near-zero refractive index photonics," Nat. Photonics **11**, 149–158 (2017).
2. N. Kinsey, C. DeVault, A. Boltasseva, and V. M. Shalaev, "Near-zero-index materials for photonics," Nat. Rev. Mater. **4**, 742–760 (2019).
3. D. I. Vulis, O. Reshef, P. Camayd-Munoz, and E. Mazur, "Manipulating the flow of light using Dirac-cone zero-index metamaterials," Rep. Prog. Phys. **82**, 012001 (2019).
4. Y. Li, C. T. Chan, and E. Mazur, "Dirac-like cone-based electromagnetic zero-index metamaterials," Light Sci. Appl. **10**, 203 (2021).
5. M. Silveirinha and N. Engheta, "Tunneling of electromagnetic energy through subwavelength channels and bends using epsilon-near-zero materials," Phys. Rev. Lett. **97**, 157403 (2006).
6. A. Alù, M. G. Silveirinha, A. Salandrino, and N. Engheta, "Epsilon-near-zero metamaterials and electromagnetic sources: tailoring the radiation phase pattern," Phys. Rev. B **75**, 155410 (2007).
7. R. Liu, Q. Cheng, T. Hand, J. J. Mock, T. J. Cui, S. A. Cummer, and D. R. Smith, "Experimental demonstration of electromagnetic tunneling through an epsilon-near-zero metamaterial at microwave frequencies," Phys. Rev. Lett. **100**, 023903 (2008).
8. H. Suchowski, K. O'Brien, J. Wong Zi, A. Salandrino, X. Yin, and X. Zhang, "Phase mismatch–free nonlinear propagation in optical zero-index materials," Science **342**, 1223–1226 (2013).
9. M. Z. Alam, I. D. Leon, and R. W. Boyd, "Large optical nonlinearity of indium tin oxide in its epsilon-near-zero region," Science **352**, 795–797 (2016).
10. J. R. Gagnon, O. Reshef, D. H. G. Espinosa, M. Z. Alam, D. I. Vulis, E. N. Knall, J. Upham, Y. Li, K. Dolgaleva, E. Mazur, and R. W. Boyd, "Relaxed phase-matching constraints in zero-index waveguides," Phys. Rev. Lett. **128**, 203902 (2022).
11. J. Xu, G. Song, Z. Zhang, Y. Yang, H. Chen, M. S. Zubairy, and S. Zhu, "Unidirectional single-photon generation via matched zero-index metamaterials," Phys. Rev. B **94**, 220103 (2016).
12. O. Mello, Y. Li, S. A. Camayd-Muñoz, C. DeVault, M. Lobet, H. Tang, M. Lončar, and E. Mazur, "Extended many-body superradiance in diamond epsilon near-zero metamaterials," Appl. Phys. Lett. **120**, 061105 (2022).
13. J. B. Khurgin and R. S. Tucker, *Slow Light: Science and Applications* (CRC Press, 2018).
14. Y. Yang, J. Lu, A. Manjavacas, T. S. Luk, H. Liu, K. Kelley, J.-P. Maria, E. L. Runnerstrom, M. B. Sinclair, S. Ghimire, and I. Brener, "High-harmonic generation from an epsilon-near-zero material," Nat. Phys. **15**, 1022–1026 (2019).
15. W. Jia, M. Liu, Y. Lu, X. Feng, Q. Wang, X. Zhang, Y. Ni, F. Hu, M. Gong, X. Xu, Y. Huang, W. Zhang, Y. Yang, and J. Han, "Broadband terahertz wave generation from an epsilon-near-zero material," Light Sci. Appl. **10**, 11 (2021).
16. E. J. Vesseur, T. Coenen, H. Caglayan, N. Engheta, and A. Polman, "Experimental verification of $n = 0$ structures for visible light," Phys. Rev. Lett. **110**, 013902 (2013).
17. Z. Zhou and Y. Li, "Effective epsilon-near-zero (ENZ) antenna based on transverse cutoff mode," IEEE Trans. Antennas Propag. **67**, 2289–2297 (2019).
18. X. Qin, W. Sun, Z. Zhou, P. Fu, H. Li, and Y. Li, "Waveguide effective plasmonics with structure dispersion," Nanophotonics **11**, 1659–1676 (2022).
19. S. Yun, Z. H. Jiang, Q. Xu, Z. Liu, D. H. Werner, and T. S. Mayer, "Low-loss impedance-matched optical metamaterials with zero-phase delay," ACS Nano **6**, 4475–4482 (2012).
20. I. Liberal, A. M. Mahmoud, Y. Li, B. Edwards, and N. Engheta, "Photonic doping of epsilon-near-zero media," Science **355**, 1058–1062 (2017).
21. H. Tang, C. DeVault, S. A. Camayd-Munoz, Y. Liu, D. Jia, F. Du, O. Mello, D. I. Vulis, Y. Li, and E. Mazur, "Low-loss zero-index materials," Nano Lett. **21**, 914–920 (2021).
22. X. Huang, Y. Lai, Z. H. Hang, H. Zheng, and C. T. Chan, "Dirac cones induced by accidental degeneracy in photonic crystals and zero-refractive-index materials," Nat. Mater. **10**, 582–586 (2011).
23. M. Dubois, C. Shi, X. Zhu, Y. Wang, and X. Zhang, "Observation of acoustic Dirac-like cone and double zero refractive index," Nat. Commun. **8**, 14871 (2017).
24. C. Xu, G. Ma, Z. G. Chen, J. Luo, J. Shi, Y. Lai, and Y. Wu, "Three-dimensional acoustic double-zero-index medium with a fourfold degenerate Dirac-like point," Phys. Rev. Lett. **124**, 074501 (2020).
25. P. Moitra, Y. Yang, Z. Anderson, I. I. Kravchenko, D. P. Briggs, and J. Valentine, "Realization of an all-dielectric zero-index optical metamaterial," Nat. Photonics **7**, 791–795 (2013).
26. Y. Li, S. Kita, P. Muñoz, O. Reshef, D. I. Vulis, M. Yin, M. Lončar, and E. Mazur, "On-chip zero-index metamaterials," Nat. Photonics **9**, 738–742 (2015).
27. L. Vertchenko, N. Akopian, and A. V. Lavrinenko, "Epsilon-near-zero grids for on-chip quantum networks," Sci. Rep. **9**, 6053 (2019).
28. T. Dong, J. Liang, S. Camayd-Munoz, Y. Liu, H. Tang, S. Kita, P. Chen, X. Wu, W. Chu, E. Mazur, and Y. Li, "Ultra-low-loss on-chip zero-index materials," Light Sci. Appl. **10**, 10 (2021).
29. L. Vertchenko, C. DeVault, R. Malureanu, E. Mazur, and A. Lavrinenko, "Near-zero index photonic crystals with directive bound states in the continuum," Laser Photonics Rev. **15**, 2000559 (2021).
30. P. Camayd-Muñoz, *Integrated Zero-index Metamaterials* (Harvard University, 2016).
31. M. Memarian and G. V. Eleftheriades, "Dirac leaky-wave antennas for continuous beam scanning from photonic crystals," Nat. Commun. **6**, 5855 (2015).
32. Q. Zhao, Z. Xiao, F. Zhang, J. Ma, M. Qiao, Y. Meng, C. Lan, B. Li, J. Zhou, P. Zhang, N. H. Shen, T. Koschny, and C. M. Soukoulis, "Tailorable zero-phase delay of subwavelength particles toward miniaturized wave manipulation devices," Adv. Mater. **27**, 6187–6194 (2015).
33. R. Peng, Z. Xiao, Q. Zhao, F. Zhang, Y. Meng, B. Li, J. Zhou, Y. Fan, P. Zhang, N.-H. Shen, T. Koschny, and C. M. Soukoulis, "Temperature-controlled chameleonlike cloak," Phys. Rev. X **7**, 011033 (2017).
34. H. Chu, Q. Li, B. Liu, J. Luo, S. Sun, Z. H. Hang, L. Zhou, and Y. Lai, "A hybrid invisibility cloak based on integration of transparent metasurfaces and zero-index materials," Light Sci. Appl. **7**, 50 (2018).
35. F. Zhang, C. Li, Y. Fan, R. Yang, N. H. Shen, Q. Fu, W. Zhang, Q. Zhao, J. Zhou, T. Koschny, and C. M. Soukoulis, "Phase-modulated scattering manipulation for exterior cloaking in metal-dielectric hybrid metamaterials," Adv. Mater. **31**, 1903206 (2019).
36. J. B. Khurgin, "Slow light in various media: a tutorial," Adv. Opt. Photonics **2**, 287–318 (2010).
37. J. B. Khurgin, M. Clerici, V. Bruno, L. Caspani, C. DeVault, J. Kim, A. Shaltout, A. Boltasseva, V. M. Shalaev, M. Ferrera, D. Faccio, and N. Kinsey, "Adiabatic frequency shifting in epsilon-near-zero materials: the role of group velocity," Optica **7**, 226–231 (2020).
38. J. B. Khurgin, M. Clerici, and N. Kinsey, "Fast and slow nonlinearities in epsilon-near-zero materials," Laser Photonics Rev. **15**, 2000291 (2020).

39. N. Xiang, Q. Cheng, J. Zhao, T. J. Cui, W. X. Jiang, and H. F. Ma, "A switchable zero index metamaterial," in *3rd Asia-Pacific Conference on Antennas and Propagation* (2014), pp. 1050–1052.

40. N. Xiang, Q. Cheng, J. Zhao, T. J. Cui, H. F. Ma, and W. X. Jiang, "Switchable zero-index metamaterials by loading positive-intrinsic-negative diodes," Appl. Phys. Lett. **104**, 053504 (2014).

41. A. R. Davoyan and N. Engheta, "Theory of wave propagation in magnetized near-zero-epsilon metamaterials: evidence for one-way photonic states and magnetically switched transparency and opacity," Phys. Rev. Lett. **111**, 257401 (2013).

42. X. Cai, R. Tang, H. Zhou, Q. Li, S. Ma, D. Wang, T. Liu, X. Ling, W. Tan, Q. He, S. Xiao, and L. Zhou, "Dynamically controlling terahertz wavefronts with cascaded metasurfaces," Adv. Photonics **3**, 036003 (2021).

43. Y. Luo, C. H. Chu, S. Vyas, H. Y. Kuo, Y. H. Chia, M. K. Chen, X. Shi, T. Tanaka, H. Misawa, Y. Y. Huang, and D. P. Tsai, "Varifocal metalens for optical sectioning fluorescence microscopy," Nano Lett. **21**, 5133–5142 (2021).

44. Q. Li, X. Cai, T. Liu, M. Jia, Q. Wu, H. Zhou, H. Liu, Q. Wang, X. Ling, C. Chen, F. Ding, Q. He, Y. Zhang, S. Xiao, and L. Zhou, "Gate-tuned graphene meta-devices for dynamically controlling terahertz wavefronts," Nanophotonics **11**, 2085–2096 (2022).

45. A. Govdeli, M. C. Sarihan, U. Karaca, and S. Kocaman, "Integrated optical modulator based on transition between photonic bands," Sci. Rep. **8**, 1619 (2018).

46. A. Gövdeli, S. Kocaman, M. Erdil, G. T. Reed, and A. P. Knights, "Tunable integrated optical modulator with dynamical photonic band transition of photonic crystals," Proc. SPIE **10923**, 109231R (2019).

47. M. Yildirim, A. Gövdeli, S. Kocaman, S. M. García-Blanco, and P. Cheben, "Integrated optical modulators with zero index metamaterials based on photonic crystal slab waveguides," Proc. SPIE **10921**, 1092125 (2019).

48. Y. Zeng, U. Chattopadhyay, B. Zhu, B. Qiang, J. Li, Y. Jin, L. Li, A. G. Davies, E. H. Linfield, B. Zhang, Y. Chong, and Q. J. Wang, "Electrically pumped topological laser with valley edge modes," Nature **578**, 246–250 (2020).

49. I. V. Shadrivov, M. Lapine, and Y. S. Kivshar, *Nonlinear, Tunable and Active Metamaterials*, Springer Series in Materials Science (Springer, 2015).

50. Z. Guo, F. Wu, C. Xue, H. Jiang, Y. Sun, Y. Li, and H. Chen, "Significant enhancement of magneto-optical effect in one-dimensional photonic crystals with a magnetized epsilon-near-zero defect," J. Appl. Phys. **124**, 103104 (2018).

51. X. Zhou, D. Leykam, U. Chattopadhyay, A. B. Khanikaev, and Y. D. Chong, "Realization of a magneto-optical near-zero index medium by an unpaired Dirac point," Phys. Rev. B **98**, 205115 (2018).

52. A. R. Davoyan and N. Engheta, "Nonreciprocal emission in magnetized epsilon-near-zero metamaterials," ACS Photonics **6**, 581–586 (2019).

53. T. Liu, N. Kobayashi, K. Ikeda, Y. Ota, and S. Iwamoto, "Topological band gaps enlarged in epsilon-near-zero magneto-optical photonic crystals," ACS Photonics **9**, 1621–1626 (2022).

54. N. Engheta, "Pursuing near-zero response," Science **340**, 286–287 (2013).

55. R. Maas, J. Parsons, N. Engheta, and A. Polman, "Experimental realization of an epsilon-near-zero metamaterial at visible wavelengths," Nat. Photonics **7**, 907–912 (2013).

56. P. Zhou, G. G. Liu, Y. Yang, Y. H. Hu, S. Ma, H. Xue, Q. Wang, L. Deng, and B. Zhang, "Observation of photonic antichiral edge states," Phys. Rev. Lett. **125**, 263603 (2020).

57. N. Wang, R.-Y. Zhang, C. T. Chan, and G. P. Wang, "Effective medium theory for a photonic pseudospin-1/2 system," Phys. Rev. B **102**, 094312 (2020).

58. D. R. Smith, J. B. Pendry, and M. C. K. Wiltshire, "Metamaterials and negative refractive index," Science **305**, 788–792 (2004).

59. S.-L. Chua, L. Lu, J. Bravo-Abad, J. D. Joannopoulos, and M. Soljačić, "Larger-area single-mode photonic crystal surface-emitting lasers enabled by an accidental Dirac point," Opt. Lett. **39**, 2072–2075 (2014).

60. P. Zhou, G. G. Liu, X. Ren, Y. Yang, H. Xue, L. Bi, L. Deng, Y. Chong, and B. Zhang, "Photonic amorphous topological insulator," Light Sci. Appl. **9**, 133 (2020).

61. D. M. Pozar, *Microwave Engineering* (Wiley, 2011).

62. L. Lu, J. D. Joannopoulos, and M. Soljačić, "Topological photonics," Nat. Photonics **8**, 821–829 (2014).

63. Q. Yan, R. Liu, Z. Yan, B. Liu, H. Chen, Z. Wang, and L. Lu, "Experimental discovery of nodal chains," Nat. Phys. **14**, 461–464 (2018).

64. H. Cheng, Y. Sha, R. Liu, C. Fang, and L. Lu, "Discovering topological surface states of Dirac points," Phys. Rev. Lett. **124**, 104301 (2020).

65. Microwave Applications Group, "Product information: microwave waveguide switches," https://www.magsmx.com/links/switch_pubA.pdf.

66. Honeywell, "Ferrite based RF switches," https://aerospace.honeywell.com/content/dam/aerobt/en/documents/learn/products/sensors/datasheet/N61-1856-000-000_FerriteBasedRFSwitching-ds.pdf.

67. Honeywell, "Ferrite beam hopping," https://aerospace.honeywell.com/content/dam/aerobt/en/documents/learn/products/sensors/datasheet/N61-1855-000-000_FerriteSwitchBeamHopper-ds.pdf.